Catalysis Science & Technology

PAPER

View Article Online
View Journal | View Issue

Cite this: *Catal. Sci. Technol.*, 2019, 9, 5745

Bi-functional $Ru/Ca_3Al_2O_6$–CaO catalyst-CO_2 sorbent for the production of high purity hydrogen *via* sorption-enhanced steam methane reforming†

Sung Min Kim, [a] Paula M. Abdala, [a] Davood Hosseini, [a] Andac Armutlulu, [a] Tigran Margossian, [b] Christophe Copéret [b] and Christoph Müller *[a]

Received 4th June 2019,
Accepted 8th September 2019

DOI: 10.1039/c9cy01095e

rsc.li/catalysis

Sorption-enhanced steam methane reforming (SE-SMR) combines steam methane reforming and a CO_2 abstraction reaction to yield high purity hydrogen. In this work, we report on the development of a bi-functional catalyst–sorbent containing Ru as the reforming catalyst and CaO as the solid CO_2 sorbent *via* a citrate sol–gel route. The material contains CaO, a structural stabilizer ($Ca_3Al_2O_6$) and Ru nanoparticles (~5 nm, 3 wt%) that are formed upon reduction in H_2. This new material was found to outperform significantly the benchmarks Ni–CaO and Ru/limestone in terms of yield of high-purity hydrogen and coke resistance. Using highly active Ru nanoparticles for the SMR allowed to maximize the weight fraction of the CO_2 sorbent CaO, hence increasing significantly the CO_2 capture capacity of the material. This favorable characteristic of the material led to an appreciably extended pre-breakthrough duration. In addition, we demonstrate that the material developed was very stable over multiple SE-SMR/regeneration cycles. The excellent cyclic stability is ascribed to the presence of $Ca_3Al_2O_6$ that stabilized effectively the porous structure of the material against sintering.

1. Introduction

Hydrogen is a carbon-free energy carrier that features a high energy density (120–142 MJ kg^{-1}).[1,2] In addition, hydrogen is also an important chemical feedstock for a number of large scale processes such as ammonia synthesis or the refining of crude oil.[3] Although its combustion does not yield any CO_2 emissions, the large scale processes through which it is currently produced, *e.g.* the steam reforming of natural gas (SMR), are energy intensive and emit large quantities of CO_2 as a side product.[4] For example, the conventional SMR process ($CH_4 + H_2O \leftrightarrows 3H_2 + CO$, $\Delta H^0_{298\ K} = 206$ kJ mol^{-1}) produces 7 kg CO_2 per kg H_2.[5] Besides the emission of CO_2, SMR is also an equilibrium limited process, *i.e.* at the SMR working a gas mixture containing approximately 76% H_2, 17% CO_2, 3% CO and 4% CH_4 is obtained.[6,7] CO is converted further with steam *via* the water gas shift reaction ($CO + H_2O \rightleftarrows CO_2 + H_2$, $\Delta H^0_{298\ K} = -41$ kJ mol^{-1}) to CO_2, yielding an additional mole of H_2 per mole CO. Unconverted CO (after the high and low temperature WGS steps) is selectively oxidized to CO_2 which is subsequently removed from the hydrogen stream by pressure swing adsorption (PSA) or amine scrubbing.[8]

The sorption-enhanced steam methane reforming (SE-SMR: $CH_4 + 2H_2O$ + sorbent $\leftrightarrows$ sorbent-$CO_2 + 4H_2$) is a promising approach to overcome the drawbacks of the traditional SMR.[9] In this process the SMR and WGS reactions proceed in the presence of a solid CO_2 sorbent. The abstraction of the product CO_2 shifts the equilibrium to the product side (Le Chatelier's principle) yielding high-purity H_2 in a single step. This allows the SE-SMR reaction to be operated also at a lower temperature of ≈550 °C compared to the conventional SMR (800–1000 °C), potentially reducing the rate of catalyst deactivation by thermal sintering.

A key component of the SE-SMR process is a CO_2 sorbent that should possess a high CO_2 uptake in the temperature range of interest (500–900 °C). In this context, CaO is a promising candidate due to (i) its high theoretical CO_2 uptake (0.78 g CO_2/g sorbent), (ii) the high abundance of its natural precursors, *e.g.*, limestone, (iii) its low CO_2 capture costs ($9–11 per ton of CO_2 captured),[10] and (iv) its fast kinetics for CO_2 uptake and release ($CaO + CO_2 \leftrightarrows CaCO_3$, $\Delta H^0_{298\ K} = -178$ kJ mol^{-1}). It is important to note that the incorporation of a

[a] *Department of Mechanical and Process Engineering, ETH Zurich, Leonhardstrasse 21, 8092 Zurich, Switzerland. E-mail: muelchri@ethz.ch*
[b] *Department of Chemistry and Applied Sciences, ETH Zurich, Vladimir Prelog Weg 1-5, 8093 Zurich, Switzerland*

† Electronic supplementary information (ESI) available. See DOI: 10.1039/c9cy01095e

CaO-based CO_2 abstraction reaction turns the highly endothermic SMR reaction into an exothermic reaction ($CH_4 + 2H_2O + CaO \leftrightarrows 4H_2 + CaCO_3$, $\Delta H^0_{298\ K} = -13$ kJ mol^{-1}).

However, the cyclic performance of CaO-based CO_2 sorbents is hampered by the low Tammann temperature of $CaCO_3$ ($T_T \approx 530$ °C) leading to sintering and in turn a loss in porosity. A high porosity is, however, required as the molar volume of the reaction product ($CaCO_3$) is almost twice as high as that of the reactant (CaO).[11,12] Therefore, to avoid that the CO_2 uptake proceeds in a slow, diffusion-limit regime (the diffusivity of CO_2 in $CaCO_3$, $D_{CaCO_3} = 0.003$ cm^2 s^{-1}, is two orders of magnitude lower than that in CaO, $D_{CaO} = 0.3$ cm^2 s^{-1}), a high porosity of the sorbent is critical. To counteract sintering, attempts have been made to stabilize the $CaCO_3$/CaO structure with high Tammann temperature metal oxides such as Al_2O_3, MgO, TiO_2, SiO_2, and ZrO_2.[13–16] As the reaction becomes diffusion-limited at a $CaCO_3$ thickness of ~50 nm,[17] also nano-structuring of the sorbent becomes an important aspect to minimize diffusion lengths.

Besides requiring a solid CO_2 sorbent, the SE-SMR relies on a SMR catalyst, typically a transition metal such as Pt, Ru, Rh, Pd, Ir, Co or Ni.[18] An additional requirement for the catalyst in the SE-SMR process is its stability in cyclic SE-SMR–regeneration. Conceptually, it is possible to simply mix a SMR catalyst with a CO_2 sorbent. However, the availability of a bi-functional material that contains both the CO_2 sorbent and the catalyst would have a number of advantages, such as enhancing heat and mass transfer and reducing the quantity of inactive support.[19,20] However, the design and manufacture of highly active and stable bi-functional materials is challenging as there is a potential for an irreversible interaction (*e.g.* formation of inactive solid solutions) between the CO_2 sorbent, the catalyst and the support.[21–23] In addition, material migration during CO_2 uptake and regeneration may block the active sites of the catalyst. In order to overcome the sintering-induced deactivation, approaches that incorporate an structural stabilizer such as $Mg_xAl_yO_z$,[24] $CaZrO_3$,[25] $Ca_{12}Al_{14}O_{33}$,[26–29] $Ca_9Al_6O_{18}$,[30] $Ca_5Al_6O_{14}$,[31] $CaAl_2O_6$ (ref. 32) have been applied to develop more effective bi-functional catalyst–sorbents. However, high metal loadings of the catalyst (15–50 wt% Ni or Co)[24,25,33] have been typically required to obtain materials with acceptable SMR activity. However, such high catalyst loadings lead to a reduced CO_2 uptake capacity per gram of material, thus, affecting negatively the economics of the SE-SMR process.

In this work, we report the development of a bi-functional material that contains Ru as the reforming catalyst and CaO as the solid CO_2 sorbent. The materials were synthesized *via* a scalable, one-pot synthesis route (citrate sol–gel method). The synthesized materials (Ru/CaO and Ru/$Ca_3Al_2O_6$–CaO) were compared to the following benchmark materials: Ru impregnated on limestone-derived CaO (Ru/lime) and a bi-functional Ni-based material (Ca–Ni-ex-Htlc).[24] The SE-SMR performance of the synthesized bi-functional materials was tested at 550 °C under equilibrium limitations (8.4 L g_{cat}^{-1} h^{-1} of GHSV, $CH_4:H_2O:N_2 = 1:4:9$). The yield of high purity hydrogen was evaluated over ten repeated cycles of SE-SMR and regeneration (at 750 °C). The stability of the materials for SE-SMR was also determined under kinetic control at 550 °C (84 L g_{cat}^{-1} h^{-1} of GHSV, $CH_4:H_2O:N_2 = 1:4:9$). The bi-functional material Ru/$Ca_3Al_2O_6$ yielded a remarkable quantity of high purity hydrogen (12–13 mmol) in the pre-breakthrough regime, outperforming the benchmark Ca–Ni-ex-Htlc and Ru/lime by more than 590%. Differences in the SE-SMR performance of the materials tested, are discussed in view of a detailed characterization of the as-synthesized and reacted materials using X-ray absorption spectroscopy (XAS), electron microscopy, X-ray powder diffraction (XRD) and N_2 physisorption.

2. Experimental

2.1. Material preparation

2.1.1. Bi-functional catalyst–sorbent. Two bi-functional Ru and CaO containing materials, referred to in the manuscript as Ru/CaO and Ru/$Ca_3Al_2O_6$–CaO, were synthesized by a citrate sol–gel route.[34] Here, citric acid (50 mmol) and ethylene glycol (30 mmol) were dissolved in 100 ml of deionized water. Subsequently calcium nitrate tetrahydrate ($Ca(NO_3)_2{\cdot}4H_2O$, Acros Organics), ruthenium nitrosyl nitrate ($Ru(NO)(NO_3)_3$, Acros Organics) and (only in the case of Ru/$Ca_3Al_2O_6$–CaO) aluminium nitrate nonahydrate ($Al(NO_3)_3{\cdot}9H_2O$, Acros Organics) were added in stoichiometric amount (total 10 mmol of metal precursors). The weight fraction of Ru was 3 wt% in both materials, and the molar ratio of Ca^{2+} : Al^{3+} in Ru/$Ca_3Al_2O_6$–CaO was 9 : 1 (as determined by ICP-OES). The solution was heated up to 110 °C under vigorous stirring until gel formation occurred. This was followed by drying at 130 °C in an oven. Subsequently, the dried materials were calcined at 850 °C (5 °C min^{-1} heating rate) for 2 h and sequentially ground and sieved to 100–300 μm. The bi-functional Ru/lime (3 wt% Ru) was prepared by wet impregnation. 1 g of Rheinkalk limestone calcined at 800 °C was added to 100 ml of an aqueous solution of ruthenium nitrosyl nitrate (3.0 mM) under vigorous stirring for 5 h. The water was evaporated subsequently in a rotary evaporator (Heidolph) at 80 °C (300 mbar). The materials were dried at 110 °C in an oven overnight, followed by calcination at 850 °C. A bi-functional material containing a Ni catalyst (45 wt% Ni, Ca–Ni-ex-Htlc) was prepared by co-precipitation and contained the following phases (after calcination): NiO, CaO and $MgAl_2O_4$. Details of its physical–chemical properties have been reported elsewhere.[24]

2.1.2. Reference materials for structural characterization. In order to provide a better understanding of the bi-functional Ru–CaO catalysts, the following reference materials were prepared for XAS and H_2-TPR measurements: (i) $CaRuO_3$ (exhibiting a perovskite structure) was prepared by a citrate sol–gel route using ruthenium nitrosyl nitrate and calcium nitrate (1 : 1 molar ratio; in total 10 mmol of metal precursors), and (ii) Ru (3 wt%) supported on γ-Al_2O_3 (Alfa Aesar) was prepared by impregnation using

$Ru(NO)(NO_3)_3$ (Acros Organics) and it is referred as Ru/Al_2O_3. The reference materials were calcined at 850 °C (5 °C min^{-1}) for 2 h. Additionally, RuO_2 (Sigma-Aldrich) with a rutile structure was used as a reference material.

2.2. Material characterization

The elemental composition of the calcined materials was determined by inductively coupled plasma optical emission spectroscopy (ICP-OES, Agilent 5100 VDV).

The surface area and pore volume of the freshly calcined and reacted materials were determined using a Quantachrome (NOVA 4000e) N_2 adsorption analyzer. Prior to N_2 adsorption, each sample was degassed at 250 °C for 3 h under vacuum (10^{-3} mbar). The Brunauer *et al.* (BET)[35] and the Barrett *et al.* (BJH) models[36] were used to calculate the surface area and pore size distribution, respectively.

Temperature-programmed reduction in H_2 (H_2-TPR) was conducted in an Autochem 2920 equipped with a thermal conductivity detector. For these measurements, 30–50 mg of the calcined catalyst was placed in a quartz reactor and heated to 300 °C in an argon atmosphere (50 mL min^{-1}) to dehydrate the sample. Next, the materials were cooled down to 50 °C and the gas was switched to 5 vol% H_2/Ar (50 mL min^{-1}). Subsequently, the temperature was increased at a rate of 5 °C min^{-1}.

Temperature-programmed oxidation (TPO) was used to determine the quantity of coke deposited on the spent catalyst. TPO experiments were performed in a thermogravimetric analyzer (TGA, Mettler Toledo TGA/DSC 3). Here, approximately 20 mg of the spent catalyst was loaded into an alumina crucible. Prior to TPO, the sample was heated to 100 °C with a heating rate of 10 °C min^{-1} in 100 mL min^{-1} of air. After a holding time of 1 h, the sample was heated further to 1000 °C (10 °C min^{-1} in 100 ml min^{-1} of air). The weight loss of the sample was continuously recorded and used to determine the mass of coke deposited.

H_2 chemisorption was carried out in an Autochem 2920 apparatus. 50–60 mg of a material was reduced in a quartz reactor at 500 °C for 1 h in 5 vol% H_2/Ar (50 mL min^{-1}). The sample was then cooled down to 400 °C and purged with Ar (50 mL min^{-1}) for 30 min. After cooling down further to 50 °C in Ar, the quantity of chemisorbed H_2 was determined by repeatedly injecting pulses of 5 vol% H_2/Ar into the reduced catalyst bed. The stoichiometry factor of dissociated H_2 to Ru was set to 1.0 (H/Ru).[37–39]

The crystalline phases in the materials were studied using an Empyrean (PANalytical) powder X-ray diffractometer operated at 40 mA and 40 kV using Cu Kα (λ = 0.1541 nm) radiation. The diffraction patterns were recorded in the range 2θ = 5–90° with 0.016° of step size.

The morphology of the samples was studied by electron microscopy (*viz.* scanning electron microscopy, SEM, FEI Magellan 400 FEG, transmission electron microscopy, TEM, Philips CM12 and FEI Talos F200X and a scanning transmission electron microscopy, STEM, Hitachi HD-2700) equipped also with an energy-dispersive X-ray (EDX) detector.

In situ X-ray absorption spectroscopy (XAS) experiments (Ru K-edge, 22.1 keV) were performed at the Swiss-Norwegian Beamlines (SNBL, BM31) of the European Synchrotron Radiation Facility (ESRF). Here, the calcined material, approximately 2 mg, was loaded in a capillary quartz reactor (1.0 mm of outer diameter) and heated up to 500 °C, with a ramp rate of 10 °C min^{-1} in 5 vol% H_2/He (10 ml min^{-1}). *Ex situ* XAS measurement were also performed on the as-synthesized materials (bi-functional materials and references). The materials were mixed with cellulose (ratio chosen such that XAS measurements in transmission mode were optimized) and ground to a fine powder. The pelletized samples were measured in transmission mode. XAS spectra were collected at the Ru K-edge using a double-crystal Si (111) monochromator (continuous scanning mode) and the data were analyzed using the Athena and Arthemis software.[40]

2.3. Cyclic CO_2 capture experiments

Cyclic CO_2 capture and regeneration experiments were performed in a TGA (Mettler Toledo TGA/DSC 3). Approximately 10 mg of the calcined material were heated to 900 °C at a heating rate of 50 °C min^{-1} under a flow of N_2 (total flow rate of 120 mL min^{-1} including a constant purge flow of N_2, 25 mL min^{-1}, over the microbalance). When the temperature of 900 °C was reached a holding time of 4 min was applied to ensure complete calcination. This was followed by a reduction of the temperature to 650 °C. At 650 °C, the CO_2 capture step was performed (20 min under 20 vol% of CO_2 in N_2, total flow rate: 150 ml min^{-1}). After carbonation, the CO_2 sorbent was regenerated at 900 °C for 10 min in a CO_2 atmosphere (30 mL min^{-1}). 10 cycles of repeated carbonation and calcination steps were performed.

The cyclic CO_2 capture performance was tested further under SE-SMR-mimicking conditions (carbonation: 550 °C using 50 ml min^{-1} of 20% CO_2/N_2, 2 h, and regeneration: 750 °C, 50 ml min^{-1} of N_2, 15 min). Prior to CO_2 capture, the calcined material was heated to 800 °C (10 °C min^{-1}) under N_2 (50 ml min^{-1}) followed by reduction at 500 °C (10 °C min^{-1}) for 2 h in 10 vol% H_2/N_2 (50 ml min^{-1}). Ten repeated cycles of carbonation (550 °C, 50 ml min^{-1} of 20 vol% CO_2/N_2) and regeneration (750 °C, 50 ml min^{-1} of N_2) were performed.

2.4. Cyclic SE-SMR experiments

The cyclic SE-SMR reaction was carried out in a fixed-bed quartz reactor (12.6 mm internal diameter and 400 mm length). 100 mg of the calcined bi-functional material (diluted with SiC with a weight ratio of 1 : 10) was used. Prior to the activity test, the bed was heated up to 800 °C (10 °C min^{-1}). A holding time of 1 h (N_2 with 100 mL min^{-1}) ensured the complete calcination of $CaCO_3$ to CaO. Subsequently, the bed temperature was reduced to 500 °C. At 500 °C the bed was treated for 2 h in 10 vol% H_2/N_2 (100 mL min^{-1}). After reduction, the SE-SMR was performed at 550 °C using a total flow rate of 14 mL min^{-1} (8.4 L g_{cat}^{-1} h^{-1} of GHSV and $CH_4 : H_2O : N_2$ = 1 : 4 : 9). After 2 h of the SE-SMR,

the bed was heated up to 750 °C (20 °C min^{-1}) in N_2 (50 ml min^{-1}) for regeneration (15 min). In total 10 cycles of SE-SMR/regeneration were performed. The composition of the off-gas (after condensation of unreacted steam) was analyzed using a micro-GC (C2V-200, Thermo Scientific) equipped with a thermal conductivity detector (TCD) and molecular sieve 5A and *U*-plot column cartridges.

3. Results and discussion

3.1. Physical–chemical and textural properties

The elemental composition determined by ICP-OES and the textural characteristics of the Ru–CaO-based materials (Ru/CaO, Ru/$Ca_3Al_2O_6$–CaO and Ru/lime) after calcination (850 °C in air) and reduction (500 °C under 10 vol% H_2/N_2) are summarized in Table 1. The elemental composition of the calcined catalysts shows a very similar loading of Ru in the materials studied here (1.6–1.7 mol% corresponding to 2.8–2.9 wt%) and is in good agreement with the desired composition. The N_2 isotherms of all of the calcined materials tested is represented well by a type III isotherm and a H3 type hysteresis loop at 0.2–0.9 of p/p^0, indicative of a randomly distributed macro-porosity (Fig. S1a†). The corresponding BJH pore size distributions show a bimodal porosity distribution with peaks located at 1.5–2.1 nm and 27.4–28.5 nm (Fig. S1b†). Overall, Ru/$Ca_3Al_2O_6$–CaO features a higher surface area and pore volume than Ru/lime and Ru/CaO (Table 1).

3.2. Structure of the calcined catalyst–sorbents and evolution upon reductive treatment

HAADF STEM images (with EDX analysis) of calcined Ru/$Ca_3Al_2O_6$–CaO showed a homogenous distribution of Ru and Al in CaO matrix (Fig. S2†).

The crystalline phases of the bifunctional catalyst–sorbents (calcined and after reduction) were characterized by XRD. All of the calcined and reduced materials contain cubic CaO ($Fm\bar{3}m$ space group), while Ru/$Ca_3Al_2O_6$–CaO contains an additional $Ca_3Al_2O_6$ ($Pa\bar{3}$) phase (Fig. 1a). Some small amounts of $Ca(OH)_2$ are also present due to the hygroscopic nature of CaO, ($Ca(OH)_2$ is formed after exposing the materials to humid air). The diffraction patterns of Ru/CaO and Ru/$Ca_3Al_2O_6$–CaO feature relatively broad peaks of CaO, characteristic of a nanostructured material. Indeed, the average crystallite sizes of CaO, calculated by the Scherrer equation,[41] are ~36 nm and ~27 nm for Ru/CaO and Ru/$Ca_3Al_2O_6$–CaO, respectively (Table 1). These values are considerably smaller than that determined for Ru/lime (~70 nm). In addition, for all of the calcined, Ru–CaO containing materials we observe additional, weak peaks that are likely due to the presence of a perovskite $CaRuO_3$ phase (*Pnma* space group, inset in Fig. 1a). However, due to the low intensity of these peaks (low Ru loading) and the overlap with other phases present, XRD provides only limited information of the Ru containing phases. Therefore, the materials were characterized further by Ru K-edge XAS to understand better the local environment of Ru after calcination and reduction (Fig. 1b) and in particular the interaction with the CO_2 capture active phase CaO.

For XAS analysis, the following reference materials were measured, and also characterized by XRD (Fig. S3†) prior to XAS analysis: (i) bulk (rutile) RuO_2 and (ii) $CaRuO_3$ which contains a pure orthorhombic perovskite phase (*Pnma* space group). In $CaRuO_3$, Ru is in an octahedral coordination, and in rutile RuO_2 in an axially elongated octahedral coordination. The X-ray absorption near edge structure (XANES) measurements acquired (Fig. 1b) show very distinct features for the $CaRuO_3$ and RuO_2 references. Both RuO_2 and $CaRuO_3$ compounds exhibit two peaks: at 22 136 and 22 149 eV, with the latter being more intense for $CaRuO_3$. Additionally, $CaRuO_3$ exhibits a feature at 22 178 eV which is absent in RuO_2. Owing to these features in the XANES signal we can distinguish between a RuO_2 or $CaRuO_3$-like local environment of Ru. For instance, in agreement with XRD, the Ru/Al_2O_3 reference shows the same XANES features as RuO_2. Turning to the bi-functional materials, the presence of features at 22 149 and 22 178 eV in Ru/lime, Ru/CaO and Ru/$Ca_3Al_2O_6$–CaO indicates that in these materials Ru is in a $CaRuO_3$-like local environment. To provide further insight into the local environment of Ru in the calcined materials, the extended X-ray absorption fine structure (EXAFS) data of the $CaRuO_3$ reference, Ru/lime, Ru/CaO and Ru/$Ca_3Al_2O_6$–CaO were fitted (Table S1 and Fig. S4†). In line with the atomic arrangement of a $CaRuO_3$ perovskite according to crystallographic data,[42] the $CaRuO_3$ reference data were fitted with a Ru–O shell at 2.0 Å, four Ru–Ca shells with

Table 1 Physical–chemical properties of the bi-functional Ru–CaO catalysts–sorbents

	Elemental composition[b]			N_2 physisorption[c]			Crystallite size[d] [nm]				
Material[a]	Ru [mol%]	Ca [mol%]	Al [mol%]	S_{BET} [m^2 g^{-1}]	V_{Pore} [cm^3 g^{-1}]	D_{pore} [nm]	CaO	Ru	Ru particle size[e] [nm]	H_2 uptake[f] [μmol_{Ru} g_{cat}^{-1}]	
Ru/lime	1.7	97.3	—	12	0.11	2.2	70	18	22.6 ± 2.6	4.8	(1.6%)
Ru/CaO	1.6	98.4	—	17	0.19	1.8	36	10	11.2 ± 2.2	18.4	(6.2%)
Ru/$Ca_3Al_2O_6$–CaO	1.7	88.6	9.7	23	0.26	1.8	27	5	5.3 ± 1.3	37.4	(12.7%)

[a] The bi-functional Ru–CaO catalyst–sorbent was calcined at 800 °C in static air and reduced in 10 vol% H_2/N_2. [b] The normalized metal mol% of Ru, Ca an Al in the calcined materials were obtained by ICP-OES. [c] Textural properties of the calcined materials. [d] Average crystallite size of CaO and Ru (in the reduced materials) determined by Scherrer's equation.[41] [e] Average Ru particle size of the reduced materials determined by TEM. [f] The quantity of surface Ru in the reduced materials as determined by H_2 chemisorption using a stoichiometry factor of 1.0 of H/Ru,[37–39] parenthesis represents Ru dispersion (%) in the reduced catalysts.

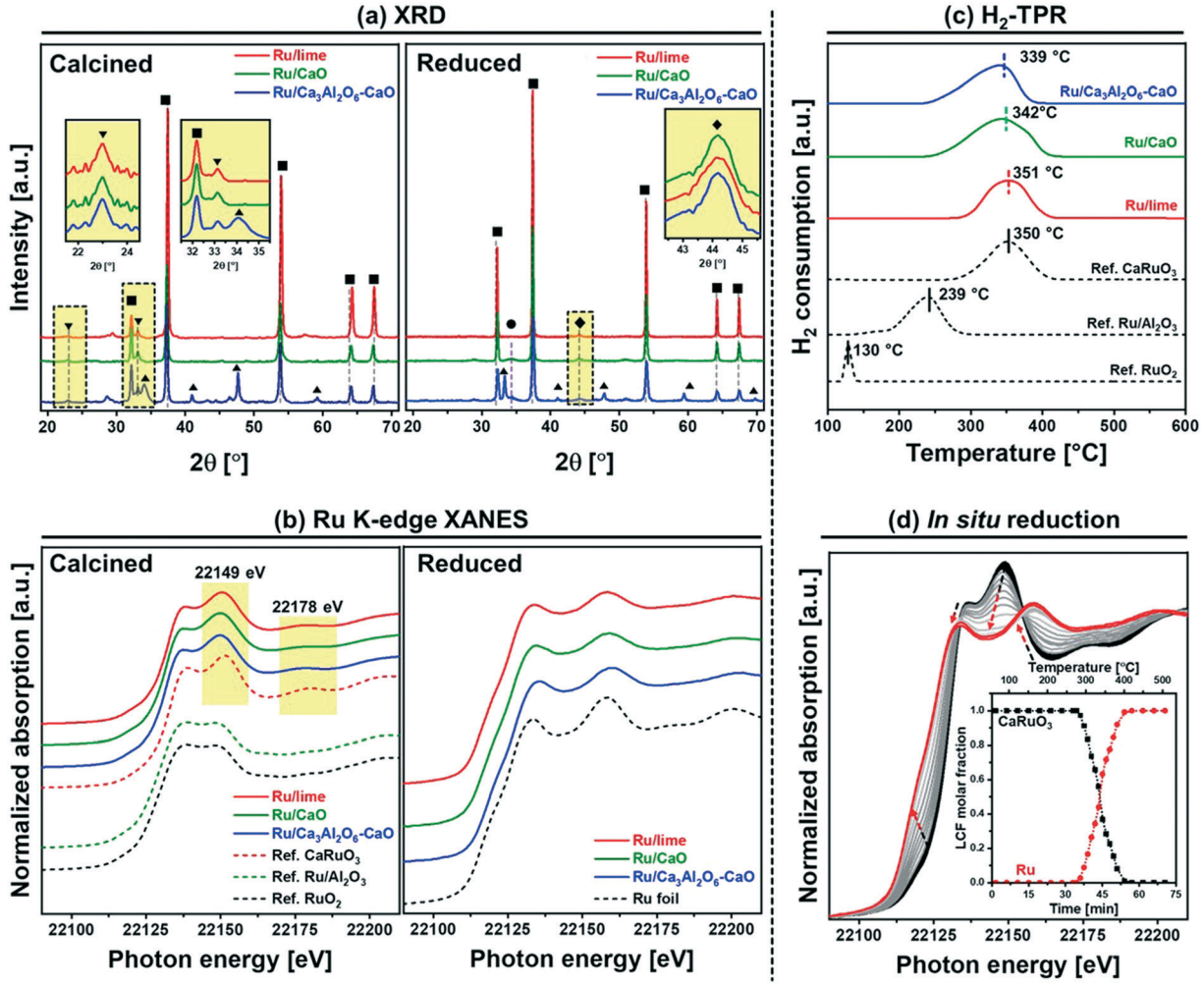

Fig. 1 Structural characterization of the calcined and reduced materials: (a) XRD of the calcined and reduced bifunctional materials. The insets show Bragg reflections due to $CaRuO_3$ and Ru, respectively. The symbols represent the following phases: (■) CaO, (▲) $Ca_3Al_2O_6$, (●) $Ca(OH)_2$, (▼) $CaRuO_3$ and (♦) Ru. (c) Ru K-edge, XANES of bifunctional materials after calcination in air at 850 °C air and reduction in 10 vol% H_2/N_2 at 500 °C. (c) H_2-TPR of bifunctional materials and references. (d) *In situ* Ru K-edge XANES spectra of $Ru/Ca_3Al_2O_6$–CaO, during temperature programed reduction in 5 vol% H_2/He. The arrows indicate the direction of change with time and temperature. The inset shows the results of the LCF analysis.

interatomic distances in the range of 3.14–3.61 Å and one Ru–Ru shell at 3.84 Å (and with coordination numbers set to the crystallographic values). The same model of the local structure of Ru was applied to Ru/lime, Ru/CaO and Ru/$Ca_3Al_2O_6$–CaO. All three Ru–CaO-based sorbents showed a Ru–O coordination sphere at interatomic distances in the range of 1.95–1.97 Å, four Ru–Ca shells with interatomic distances in the range of 3.10–3.47 Å and a Ru–Ru shell at 3.76–3.87 Å. These results are in line with the XANES observation that suggests Ru has a local environment consistent with $CaRuO_3$. On the other hand, the Debye Waller factors observed for the synthetic materials were larger than for the reference crystalline perovskite. This can be explained by a higher disorder of the local environmental of Ru in a highly dispersed $CaRuO_3$-phase within the CaO or CaO–$Ca_3Al_2O_6$ matrix.

The reduction characteristics of the different materials (bi-functional materials and references) were assessed by H_2-TPR experiments (Fig. 1c) after calcination (in air) at 800 °C. The diffractogram of the calcined materials (Fig. 1a) confirmed that there was no $CaCO_3$ in the samples. In addition, all H_2-TPR profiles showed a stable baseline between 600–1000 °C (without any further H_2 consumption). The TPR profile of the reference bulk RuO_2 shows a reduction peak at 130 °C, in agreement with literature.[43] On the other hand, Ru/Al_2O_3 show higher reduction temperatures, *viz.* 239 °C. In agreement with literature.[44,45] The reference $CaRuO_3$ shows a reduction peak at 350 °C, according to: $CaRuO_3 + 2H_2 \rightarrow Ru^0 + CaO + 2H_2O$. All the Ru–CaO-containing materials (Ru/lime, Ru/CaO and Ru/$Ca_3Al_2O_6$–CaO) show a reduction peak in the temperature range 339–351 °C (similar to $CaRuO_3$) indicating that Ru^0 is obtained through the reduction of a $CaRuO_3$ phase. The TPR experiments were complemented with *in situ* Ru K-edge XANES (Fig. 1d). Linear combination fitting (LCF) using Ru foil, RuO_2 and $CaRuO_3$ as references allowed us to quantify

the evolution of these phases in Ru/$Ca_3Al_2O_6$–CaO (Fig. 1d) during *in situ* XANES TPR. Our XANES analysis shows that $CaRuO_3$ reduces to Ru^0 between 260–400 °C. We could not detect any intermediate phases or segregation of RuO_2.

Additionally, using *ex situ* XRD analysis, the formation of metallic Ru particles after reduction at 500 °C in 10 vol% H_2/N_2 is evidenced by the appearance of, albeit weak, (101) reflections due to hexagonal Ru ($P6_3/mmc$ space group) at ~44° (Fig. 1a). This Bragg reflection is observed in all of the Ru containing materials. Using Scherrer's equation, the average Ru crystallite sizes were estimated as: Ru/lime (18 nm) > Ru/CaO (10 nm) > Ru/$Ca_3Al_2O_6$–CaO (5 nm).

H_2 chemisorption was employed to quantify the amount of surface Ru (Table 1). Considering a stoichiometry factor of 1.0 of H/Ru,[37–39] the quantity of surface Ru and its dispersion were determined as follows: 4.8 $\mu mol_{Ru}\ g_{cat}^{-1}$ and 1.6% (Ru/lime) < 18.4 $\mu mol_{Ru}\ g_{cat}^{-1}$ and 6.2% (Ru/CaO) < 37.4 $\mu mol_{Ru}\ g_{cat}^{-1}$ and 12.7% (Ru/$Ca_3Al_2O_6$–CaO).

HR-SEM and HAADF-STEM images of the reduced materials are shown in Fig. 2. In HR-SEM (Fig. 2a), reduced Ru/$Ca_3Al_2O_6$–CaO exhibits particles of CaO or $Ca_3Al_2O_6$ with an average size of 90 ± 10 nm, which is a factor of 1.6–2.0 smaller than the size observed in Ru/CaO (140 ± 20 nm) and Ru/lime (170 ± 40 nm). Ru nanoparticle were observed by HAADF STEM in all of the materials (Fig. 2b and c) with average sizes determined as: 22.6 ± 2.6 nm (Ru/lime) > 11.2 ± 2.2 nm (Ru/CaO) > 5.3 ± 1.3 nm (Ru/$Ca_3Al_2O_6$–CaO). Hence

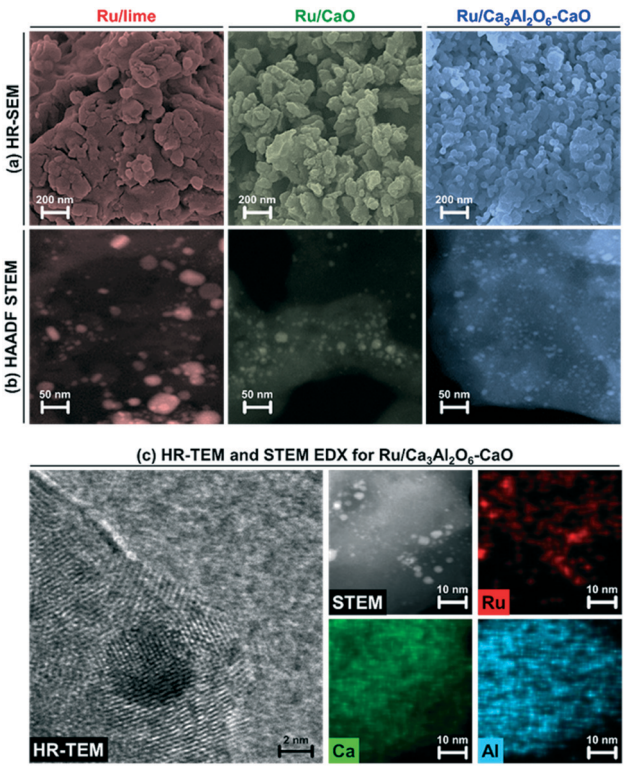

Fig. 2 Electron microscopy based characterization of the reduced materials: (a) HR-SEM and (b) HAADF-STEM of reduced Ru/lime, Ru/CaO and Ru/$Ca_3Al_2O_6$–CaO. (c) HR-TEM and STEM EDX mapping for reduced Ru/$Ca_3Al_2O_6$–CaO.

electron microscopy, in combination with H_2 chemisorption measurements, show that the one-pot, citrate sol–gel method (Ru/CaO and Ru/$Ca_3Al_2O_6$–CaO) leads to smaller Ru nanoparticles compared to impregnation (Ru/lime), yielding in turn a higher quantity of Ru surface sites.

3.3. CO_2 capture performance

The cyclic CO_2 capture performance of the bi-functional catalyst–sorbents (Ru/CaO, Ru/$Ca_3Al_2O_6$–CaO and the benchmarks Ru/lime and Ca–Ni-ex-Htlc) was assessed in a TGA (carbonation was performed in 20% CO_2/N_2 at 650 °C and calcination in CO_2 at 900 °C, Fig. 3a). The CO_2 uptake in the 1st cycle decreases in the following order: Ru/CaO (0.57 g_{CO_2}/g) > Ru/$Ca_3Al_2O_6$–CaO (0.54 g_{CO_2}/g) > Ru/lime (0.45 g_{CO_2}/g) ≫ Ca–Ni-ex-Htlc (0.11 g_{CO_2}/g). The reference material Ca–Ni-ex-Htlc has a comparatively low CO_2 uptake, owing to the high content of Ni (45 wt%). After 10 cycles of repeated carbonation–calcination, the CO_2 uptake of Ru/CaO and Ru/lime has reduced appreciably to 0.16 $g_{CO_2}\ g_{cat}^{-1}$ and 0.15 $g_{CO_2}\ g_{cat}^{-1}$, corresponding to a capacity retention of 31% and 33%, respectively. On the other hand, a significantly higher cyclic stability was observed for Ru/$Ca_3Al_2O_6$–CaO and Ca–Ni-ex-Htlc, yielding a CO_2 uptake of 0.46 g_{CO_2}/g and 0.09 g_{CO_2}/g, respectively (corresponding to capacity retentions of respectively, 92% and 82% after 10 cycles). These findings indicate that the presence of a high Tammann temperature stabilizer, *viz.* $Ca_3Al_2O_6$ (T_T = 771 °C) or $MgAl_2O_4$ (T_T = 1065 °C) in, respectively, Ru/$Ca_3Al_2O_6$–CaO and Ca–Ni-ex-Htlc, improves the cyclic stability over ten cycles of the CO_2 uptake in these materials (although the CaO content in Ca–Ni-ex-Htlc is rather low, *i.e.* 21 wt%), in agreement with previous studies.[13]

Temporally resolved carbonation profiles were acquired for each material to elucidate the origin of deactivation upon cyclic operation. Fig. 3b plots the CO_2 uptake of a series of materials in the 1st and 10th carbonation cycle as a function of time. The carbonation of CaO is known to occurs in two regimes:[17,46] i) a reaction stage that is kinetically controlled and in which $CaCO_3$ fills the volume available in small pores (d_{pore} < 100 nm) and ii) a diffusion-limited reaction stage that is controlled by the slow diffusion of CO_2 through the $CaCO_3$ product layer. The diffusivity of CO_2 through $CaCO_3$ (D_{CaCO_3} = 0.003 $cm^2\ s^{-1}$) is significantly smaller than its diffusion through CaO (D_{CaO} = 0.3 $cm^2\ s^{-1}$).[47] Here, we determine the transition between these two reaction stages as the intersection of two lines that fit linearly the CO_2 uptake with time in the two carbonation regimes. Owing to the large difference in the rate of carbonation in the two reaction regimes, a large fraction of the overall CO_2 uptake occurs in the kinetically-controlled regime, *viz.* 0.40 g_{CO_2}/g, 0.35 g_{CO_2}/g and 0.33 g_{CO_2}/g for, respectively, Ru/lime, Ru/CaO and Ru/$Ca_3Al_2O_6$–CaO, in 1st cycle (contributing to 88%, 62% and 63% of the respective overall CO_2 uptake). However, after two cycles, the CO_2 uptake of Ru/CaO and Ru/lime in the kinetically-controlled reaction stage decreased significantly to 0.19 g_{CO_2}/g and 0.21 g_{CO_2}/g, *i.e.*, a reduction by 45% and 48%,

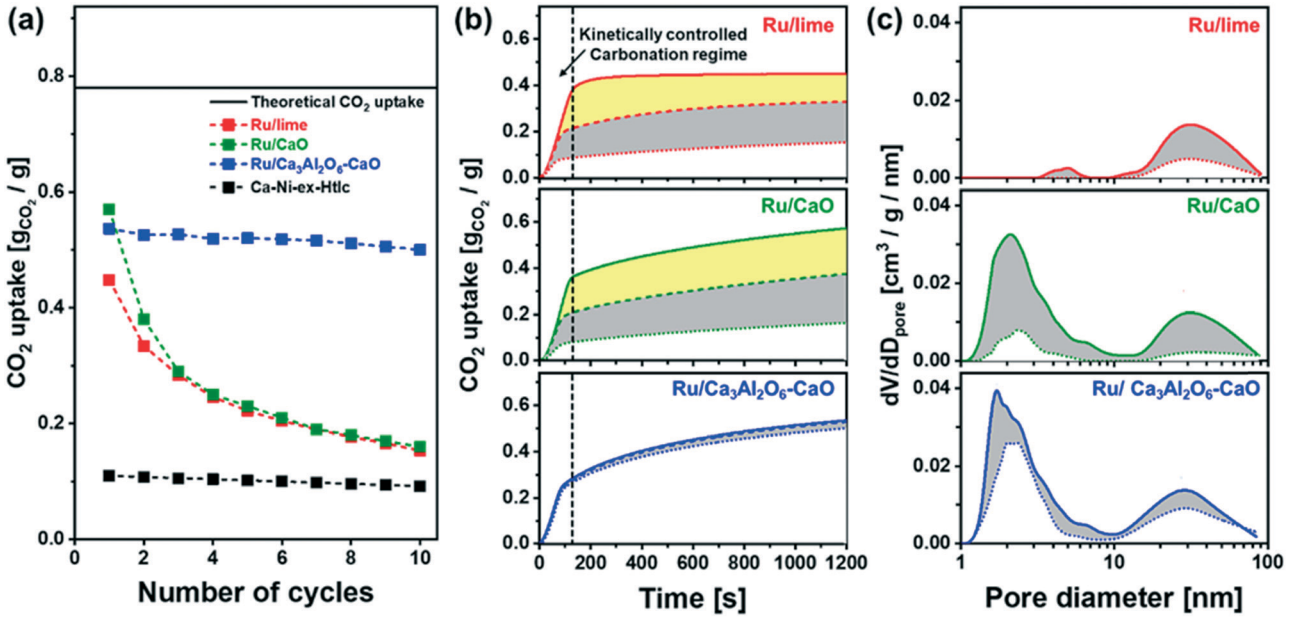

Fig. 3 CO_2 capture: (a) CO_2 uptake as a function of number of carbonation–regeneration cycles. The solid line is the theoretical CO_2 uptake of pure CaO, *i.e.*, 0.78 g_{CO_2}/g. (b) CO_2 uptake *vs.* carbonation time. The solid dashed and dotted lines represent the 1st, 2nd and 10th carbonation cycle, respectively. The reduction in the CO_2 uptake is highlighted by grey and yellow fills. (c) BJH pore size distribution of freshly calcined (dash line) materials and materials that have undergone 10 cycles (dotted line) of carbonation and regeneration (calcined form). The reduction in pore volume over 10 cycles is highlighted by a grey fill.

respectively (these values reduced to 0.10 g_{CO_2}/g and 0.08 g_{CO_2}/g after 10 cycles). The decrease in the CO_2 uptake is significantly less pronounced in Ru/$Ca_3Al_2O_6$–CaO which can be attributed to a reduction in the extent of sintering due to the presence of the stabilizer $Ca_3Al_2O_6$.

Changes in the porosity of the materials with cyclic operation were monitored by N_2 adsorption. The pore size distribution of the freshly calcined materials and materials that have been exposed to 10 cycles of carbonation and regeneration are plotted in Fig. 3c (values given in Table S2†). In Ru/lime and Ru/CaO the pore volume in pores with a diameter <100 nm was reduced appreciably over 10 cycles of carbonation and regeneration, *viz.* from 0.11 cm^3 g^{-1} to 0.01 cm^3 g^{-1} and from 0.19 cm^3 g^{-1} to 0.05 cm^3 g^{-1}, respectively. On the other hand, Ru/$Ca_3Al_2O_6$–CaO retains to a larger extend its pore volume (0.23 cm^3 g^{-1} after 10 cycles of carbonation and regeneration compared to an initial value of 0.26 cm^3 g^{-1}). The reduction in pore volume (d_{pore} < 100 nm), highlighted in gray in Fig. 3c, agrees well with the trend observed for the decay of the CO_2 uptake in the kinetically controlled regime (Fig. S5†). This observation is in line with the hypothesis that the CO_2 uptake in the kinetically-controlled regime is linked directly to the pore volume available in pores with d_{pore} < 100 nm.[48,49]

3.4. SE-SMR performance: first cycle

In the following the SE-SMR activity of the materials synthesized was assessed at 550 °C using a feed composition of CH_4 : H_2O : N_2 = 1 : 4 : 9 (total flow rate 14 ml min^{-1}; GHSV = 8.4 L g_{cat}^{-1} h^{-1}). Fig. 4 summarizes the results of the Ru containing materials, whereas the activity of the benchmark Ca–Ni-ex-Htlc is plotted in Fig. S6a.† Fig. 4a plots the SE-SMR performance of Ru/lime, Ru/CaO and Ru/$Ca_3Al_2O_6$–CaO (N_2-free off-gas composition on a dry basis) in the 1st cycle. Generally, the SE-SMR reaction can be divided into three reaction stages. In the so-called pre-breakthrough stage (labelled i, Fig. 4a), high-purity H_2 is produced. This stage is followed by a breakthrough stage (labelled ii) in which there is some CH_4 slip. In addition, also CO_2 and CO are detected in the effluent gas. In the post-breakthrough stage (labelled iii), the concentrations of CH_4, CO, CO_2 and H_2 approach the equilibrium concentration of the conventional SMR, as the CO_2 sorbent has been converted by a large extent to $CaCO_3$. The exception from this reaction pattern is Ru/lime which shows a continuously increasing concentration of CH_4, without any clear pre-breakthrough stage, indicative of a very poor SMR activity of this material. This is most likely due to the large Ru particle size and hence the low dispersion of Ru in this material (Table 1). On the other hand, Ru/CaO and Ru/$Ca_3Al_2O_6$–CaO, show clearly all three reaction stages, indicative of a high catalytic activity of these two materials. For Ru/CaO, the mole fraction of CO_2, CO and CH_4 in the pre-breakthrough stage (t = 0–83 min for the 1st cycle) are very low (<0.03) yielding a H_2 mole fraction of ≈0.97, which is close to the thermodynamic equilibrium (0.99) of the SE-SMR, and significantly higher than the thermodynamic equilibrium of the conventional SMR (0.75). This result implies that the CO_2 that is produced during the simultaneous SMR and WGS reactions is immediately

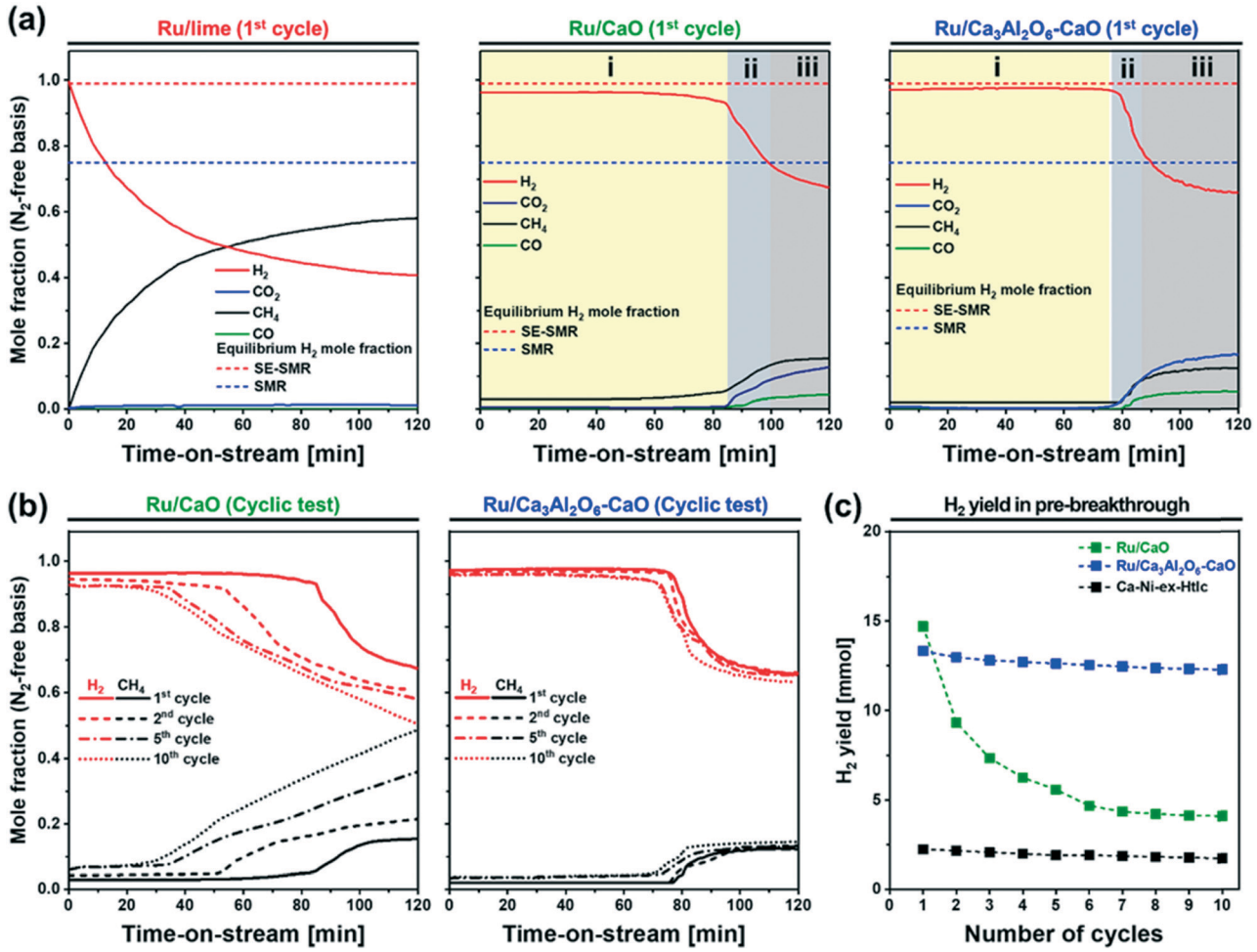

Fig. 4 SE-SMR performance: off-gas composition for Ru/lime, Ru/CaO and Ru/$Ca_3Al_2O_6$–CaO in the 1st cycle. Three reaction stages can be identified in the SE-SMR step: (i) pre-breakthrough, (ii) breakthrough, and (iii) post-breakthrough stage. (b) Breakthrough curves of H_2 and CH_4 for Ru/CaO and Ru/$Ca_3Al_2O_6$–CaO in the 1st, 5th and 10th cycles. (c) The H_2 yield as a function of number of repeated SE-SMR–regeneration cycles.

captured by CaO, *i.e.*, CaO + CO_2 → $CaCO_3$. In the post-breakthrough stage, the mole fraction of CO_2 in the off gases increases (0.18) while the mole fraction of H_2 decreases (0.67). The three characteristic stages of the SE-SMR are also observed for Ru/$Ca_3Al_2O_6$–CaO, yet the duration of the pre-breakthrough period is slightly shorter (t = 0–70 min) than for Ru/CaO. The most likely explanation for this observation is the lower content of CaO in this material due to the formation of CO_2-capture-inactive $Ca_3Al_2O_6$ (the CO_2 uptake of Ru/CaO and Ru/$Ca_3Al_2O_6$–CaO in the first cycle was 0.57 g_{CO_2}/g and 0.54 g_{CO_2}/g, respectively). The benchmark Ca–Ni-ex-Htlc has a significantly shorter pre-breakthrough period (t = 0–13 min) as this material contains 45 wt% Ni and only 21 wt% CaO (Fig. S6a†), hence possessing a lower CO_2 uptake capacity.

3.5. SE-SMR performance: cyclic performance

Fig. 4b and S6b† plot the SE-SMR performance of Ru/CaO, Ru/$Ca_3Al_2O_6$–CaO and Ca–Ni-ex-Htlc as a function of cycle number (1, 2, 5 and 10 cycles). Ru/CaO shows a decreasing H_2 purity in the pre-breakthrough stage over 10 cycles (decrease from 96 to 92 mole%) and a continuous increase of the concentration of CH_4 at the end of post-breakthrough stage (increase from 15 to 49 mole% over 10 cycles). Moreover, for Ru/CaO the time on stream when breakthrough occurs decreases with cycle number from 83 min (1st cycle) to 53 min, 33 min and 25 min in the 2nd, 5th and 10th cycles, respectively. On the other hand, a higher cyclic stability, *i.e.* a reduced decline in the duration of the pre-breakthrough period with cycle number, is observed for Ru/$Ca_3Al_2O_6$–CaO. After 10 cycles, Ru/$Ca_3Al_2O_6$–CaO and Ca–Ni-ex-Htlc retained, respectively, 92% and 76%, of the duration of the initial pre-breakthrough period compared to 29% for Ru/CaO.

Two reasons could lead to a deactivation of the materials with cycle number *viz.* catalyst deactivation or a reduction in the CO_2 uptake capacity of the sorbent (or a combination of both effects). To obtain further insight into the cause(s) of material deactivation and to explain the improved stability of Ru/$Ca_3Al_2O_6$–CaO, we investigate: 1) whether there exists a correlation between the SE-SMR performance and changes in

the CO_2 uptake capacity of the materials with cycle number, 2) the catalytic stability far from equilibrium conversion, 3) changes in the morphology of the materials and 4) the quantity of coke deposited.

3.5.1. Correlation between SE-SMR performance and CO_2 uptake. Fig. 4c plots the quantity of H_2 produced in the pre-breakthrough stage as a function of cycle number for the different materials studied. Generally, the bi-functional, Ru–CaO-based materials show a higher yield of H_2 than the benchmark Ca–Ni-ex-Htlc, due to their higher CaO content and hence extended pre-breakthrough period. Nonetheless, also Ru/CaO and Ru/$Ca_3Al_2O_6$–CaO show a reduction in the duration of the pre-breakthrough period with cycle number. Fig. 5a plots the H_2 yield in the pre-breakthrough period against the CO_2 uptake for a given cycle number determined under SE-SMR mimicking conditions (Fig. S7†). This plot indicates that there is indeed a linear correlation between the CO_2 uptake and the duration of the pre-breakthrough period, hence, also the yield of high purity hydrogen.

3.5.2. SE-SMR performance in the kinetic regime. To probe material stability further, the SE-SMR reaction was also performed in the kinetic regime, far from equilibrium conversions (*i.e.* at a CH_4 conversion of 40% as opposed to 98% for equilibrium conditions). Specifically, the SE-SMR was operated at 550 °C with a high GHSV of 84.0 L g_{cat}^{-1} h^{-1} (140 ml min^{-1} of 10 CH_4/40 H_2O/90 N_2). Fig. 5b plots the rate of methane consumption (after 1 h TOS) normalized by surface Ru (quantified by H_2 chemisorption using a stoichiometric factor of $H/M_{(Ni\ or\ Ru)}$ = 1.0). For the different materials tested, the rate of CH_4 consumption in the post-breakthrough regime (after 1 h TOS) in the first cycle shows a linear relationship with the quantity of surface Ru, indicating that surface metallic Ru is the active sites for SMR. The normalized rate of CH_4 consumption (1 h of TOS) for the Ru–CaO-based materials is in the range 5–5.4 mol_{CH_4} mol_{Ru}^{-1} s^{-1}, which is approximately 50% higher than for the Ca–Ni-ex-Htlc benchmark (3.6 mol_{CH_4} mol_{Ni}^{-1} s^{-1}). The higher activity of Ru for the SMR compared to Ni is in line with previous findings.[50] After 10 cycles, Ru/$Ca_3Al_2O_6$–CaO demonstrated a high catalytic stability, *viz.* the rate of the normalized methane consumption (4.2 mol_{CH_4} mol_{Ru}^{-1} s^{-1}) exceeded substantially the values of Ru/lime (0.7 mol_{CH_4} mol_{Ru}^{-1} s^{-1}) and Ru/CaO (0.8 mol_{CH_4} mol_{Ru}^{-1} s^{-1}). Nevertheless, a gradual reduction of the normalized rate of methane consumption with cycle number was observed for Ru/$Ca_3Al_2O_6$–CaO (Fig. 5c), pointing to a deactivation of the catalyst.

3.5.3. Characterization of bifunctional Ru–CaO materials after cyclic SE-SMR reaction. Textural changes over repeated SE-SMR cycles were probed by N_2 adsorption (Table S3 and Fig. S8†). In particular, the Al-free materials show an appreciable reduction in the pore volume and surface area, *viz.* S_{BET} = 5 m^2 g_{cat}^{-1} and V_{pore} = 0.06 cm^3 g_{cat}^{-1} for Ru/lime and S_{BET} = 6 m^2 g_{cat}^{-1} and V_{pore} = 0.07 cm^3 g_{cat}^{-1} for Ru/CaO. On the other hand, the textural characteristics of Ru/$Ca_3Al_2O_6$–CaO are largely maintained (S_{BET} = 18 m^2 g_{cat}^{-1} and V_{pore} = 0.21 cm^3 g_{cat}^{-1} after 10 cycles of SE-SMR compared to the initial values of S_{BET} = 23 m^2 g_{cat}^{-1} and V_{pore} = 0.26 cm^3 g_{cat}^{-1}). The substantial changes in the textural properties of Ru/lime and Ru/CaO with repeated SE-SMR/regeneration cycles are also visualized by HR-SEM (Fig. 6a).

Turning to the growth of the Ru nanoparticles, analysis of HAADF STEM images (freshly reduced, Fig. 2, and spent materials, Fig. 6b) reveals an increase in the size of the Ru particle size from 5.3 ± 1.3 nm to 8.4 ± 2.0 nm for Ru/$Ca_3Al_2O_6$–CaO after 10 cycles (Fig. 6c). However, this particle size is still 2.7 and 4.0 times smaller than that of spent Ru/CaO (22.5 ± 4.2 nm) and Ru/lime (33.5 ± 3.6 nm), respectively. The trend in the Ru particle size as determined by HAADD STEM is in good agreement with the trend in surface Ru as quantified by H_2 chemisorption (Table S3†): Ru/$Ca_3Al_2O_6$–CaO (31.5 μmol_{Ru} g_{cat}^{-1}) > Ru/CaO (7.2 μmol_{Ru} g_{cat}^{-1}) > Ru/lime (2.1 μmol_{Ru} g_{cat}^{-1}). These measurements provide strong evidence that the decrease in the rate of methane consumption is due to the sintering of Ru particles.

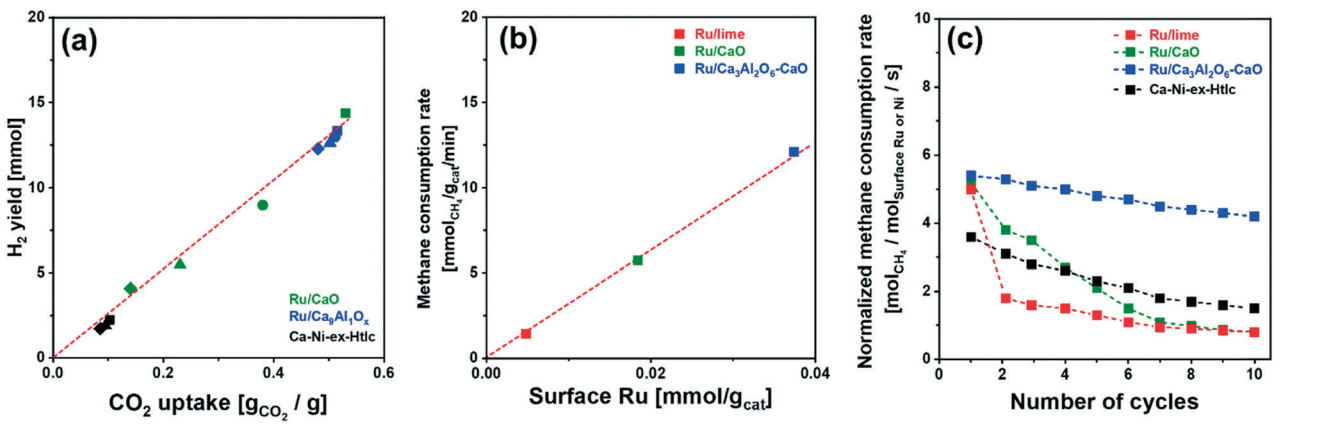

Fig. 5 H_2 yield and CH_4 consumption rate: (a) H_2 yield in the pre-breakthrough period as a function of the CO_2 uptake for the materials studied at different cycle numbers: (■) 1st, (●) 2nd, (▲) 5th and (◆) 10th cycle (reported in Fig. S7†); (b) the rate of CH_4 consumption (after 1 h of TOS) as a function of the quantity of surface Ru. (c) Rate of CH_4 consumption, normalized by surface Ru or Ni, in the post-breakthrough stage of the SE-SMR reaction at 550 °C (total flow rate of 140 ml min^{-1} with a composition of 10 CH_4/40 H_2O/90 N_2; GHSV = 84.0 L g_{cat}^{-1} h^{-1}).

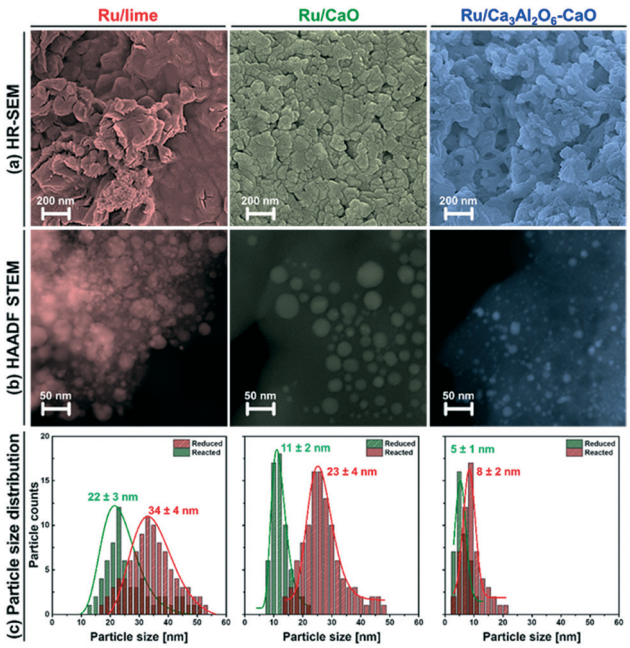

Fig. 6 Electron microscopy-based characterization of the spent bi-functional materials: (a) HR-SEM, (b) HAADF-STEM and (c) particle size distribution of Ru/lime, Ru/CaO and Ru/$Ca_3Al_2O_6$–CaO after exposure to 10 SE-SMR/regeneration cycles.

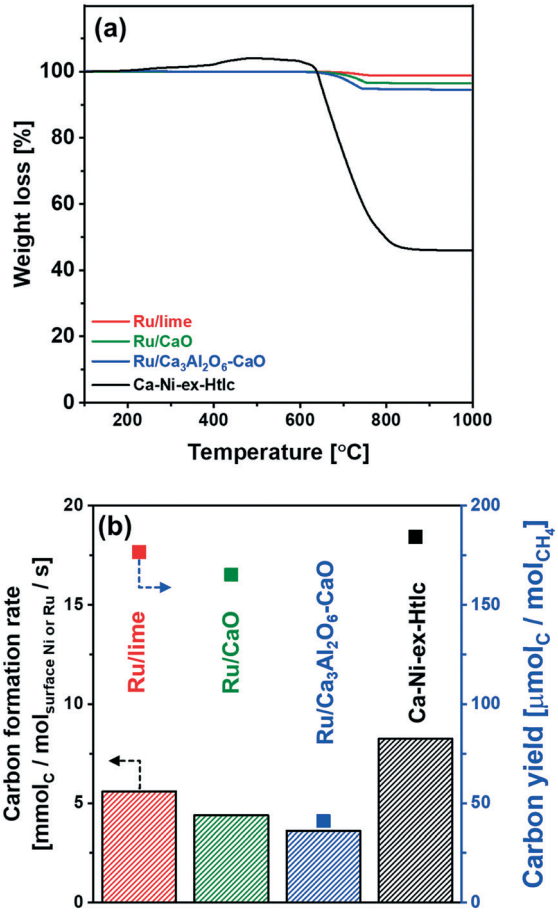

Fig. 7 Coke formation: (a) TPO analysis of the spent materials in a TGA. Weight loss after TPO treatment is given in parenthesis. (b) Average rate of carbon deposition normalized by surface Ru or Ni, and carbon yield determined as mole of accumulated carbon per mole of reacted CH_4 over 10 SE-SMR/regeneration cycles.

3.5.4. Extent of coke formation. To probe the extend of coke formation, materials that have undergone 10 SE-SMR/regeneration cycles were collected (after the SE-SMR step) and characterized by TPO (Fig. 7a). The weight increase of Ca–Ni-ex-Htlc in the temperature range 300–500 °C is due to the oxidation of Ni to NiO. On the other hand, the weight increase of Ru-containing materials in the temperature range 100–600 °C was negligible. The weight loss due to the oxidation of carbonaceous species occurs in the temperature ranges of 650–750 °C and 610–850 °C for Ru–CaO-containing materials and Ca–Ni-ex-Htlc, respectively. The quantity of carbon deposited increased in the following order: Ru/Lime (1.1 wt%) < Ru/CaO (3.4 wt%) < Ru/$Ca_3Al_2O_6$–CaO (5.4 wt%) ≪ Ca–Ni-ex-Htlc (56.2 wt%). The small amount of carbon deposited on Ru/lime is probably due to the rather poor SMR activity of this material. Fig. 7b plots the carbon yield, *i.e.* the accumulated amount of carbon per mole of reacted CH_4 over 10 SE-SMR/regeneration cycles. Ru/$Ca_3Al_2O_6$–CaO showed a significantly lower carbon yield (41 $\mu mol_C\ mol_{CH_4}^{-1}$) compared to Ru/CaO (165 $\mu mol_C\ mol_{CH_4}^{-1}$), Ru/lime (177 $\mu mol_C\ mol_{CH_4}^{-1}$) and Ca–Ni-ex-Htlc (184 $\mu mol_C\ mol_{CH_4}^{-1}$). Furthermore, the rate of carbon formation normalized by surface Ni or Ru (as determined by chemisorption, Fig. 7b) shows the following trends: Ru/$Ca_3Al_2O_6$–CaO (3.6 $mmol_C\ mol_{Ru}^{-1}\ s^{-1}$) < Ru/CaO (4.4 $mmol_C\ mol_{Ru}^{-1}\ s^{-1}$) < Ru/lime (5.6 $mmol_C\ mol_{Ru}^{-1}\ s^{-1}$) ≪ Ca–Ni-ex-Htlc (8.2 $mmol_C\ mol_{Ni}^{-1}\ s^{-1}$). Carbon formation is favored at step and edge sites of metallic Ni and Ru, which are dominant in large particles (>5 nm).[51,52] Hence, the higher amount of coke deposited on Ru/lime and Ca–Ni-ex-Htlc, when compared to Ru/CaO and Ru/$Ca_3Al_2O_6$–CaO, is due to the larger Ru and Ni particles in these systems. Hence, bi-functional, Ru-based materials allow a significant reduction of the loading of the active catalyst, and hence a higher fraction of CaO, but also reduce the extent of carbon formation. However, the high costs of Ru are a disadvantage.

4. Conclusions

We have developed a highly active and stable, Ru/$Ca_3Al_2O_6$–CaO bi-functional SE-SMR material. XRD and XAS measurements of the as-synthesized (calcined) materials showed the formation of mixed oxides between CaO and the stabilizer, *viz.* $Ca_3Al_2O_6$ and the catalyst, *i.e.* $CaRuO_3$. *In situ* XAS measurements complemented by H_2-TPR and XRD revealed the formation of metallic Ru upon reduction. Owing to the high activity of Ru for the SE-SMR, the fraction of CO_2-capture-active CaO could be increased significantly when compared to the benchmark Ca–Ni-ex-Htlc, extending the pre-breakthrough duration and the yield of high-purity H_2. The presence of $Ca_3Al_2O_6$ in the material stabilized effectively the

material against sintering. Furthermore, Ru/$Ca_3Al_2O_6$–CaO showed very little coke formation when compared to Ca–Ni-ex-Htlc. Nonetheless, the high costs of Ru are a disadvantage and further work shall concentrate on reducing further the quantity of Ru in the material while maintaining its high activity.

Conflicts of interest

There are no conflicts to declare.

Acknowledgements

The authors acknowledge the financial support of ETH (ETH 57 12-2) and the Swiss National Science Foundation (200020_156015). The benchmark Ca–Ni-ex-Htlc was developed by Marcin Broda. We also thank the Scientific Center for Optic and Electron Microscopy (ScopeM) at ETH Zürich for providing access to electron microscopes and the Swiss Norwegian Beamline for access and help during XAS measurements. We thank Agnieszka Kierzkowska for ICP-OES measurements and Wouter van Beek for assistance during XAS measurements.

References

1 J. M. Ogden, M. M. Steinbugler and T. G. Kreutz, *J. Power Sources*, 1999, **79**, 143–168.
2 A. Midilli, M. Ay, I. Dincer and M. A. Rosen, *Renewable Sustainable Energy Rev.*, 2005, **9**, 255–271.
3 R. Ramachandran and R. K. Menon, *Int. J. Hydrogen Energy*, 1998, **23**, 593–598.
4 K. S. Santhanam, R. J. Press, M. J. Miri, A. V. Bailey and G. A. Takacs, *Introduction to hydrogen technology*, John Wiley & Sons, Hoboken, NJ, 2017.
5 R. Soltani, M. A. Rosen and I. Dincer, *Int. J. Hydrogen Energy*, 2014, **39**, 20266–20275.
6 M. J. Tuinier, H. P. Hamers and M. van Sint Annaland, *Int. J. Greenhouse Gas Control*, 2011, **5**, 1559–1565.
7 J. R. Rostrup-Nielsen, *Catal. Today*, 1993, **18**, 305–324.
8 J. C. Meerman, E. S. Hamborg, T. van Keulen, A. Ramírez, W. C. Turkenburg and A. P. C. Faaij, *Int. J. Greenhouse Gas Control*, 2012, **9**, 160–171.
9 A. Lopez Ortiz and D. P. Harrison, *Ind. Eng. Chem. Res.*, 2001, **40**, 5102–5109.
10 J. A. Ober, *Mineral commodity summaries 2016*, USGS, Reston, VA, 2016.
11 D. Alvarez and J. C. Abanades, *Energy Fuels*, 2005, **19**, 270–278.
12 P. Sun, J. R. Grace, C. J. Lim and E. J. Anthony, *AIChE J.*, 2007, **53**, 2432–2442.
13 S. M. Kim, W.-C. Liao, A. M. Kierzkowska, T. Margossian, D. Hosseini, S. Yoon, M. Broda, C. Copéret and C. R. Müller, *Chem. Mater.*, 2018, **30**, 1344–1352.
14 A. Armutlulu, M. A. Naeem, H.-J. Liu, S. M. Kim, A. Kierzkowska, A. Fedorov and C. R. Müller, *Adv. Mater.*, 2017, **29**, 1702896.
15 M. Broda, A. M. Kierzkowska and C. R. Müller, *Adv. Funct. Mater.*, 2014, **24**, 5753–5761.
16 S. M. Kim, A. M. Kierzkowska, M. Broda and C. R. Müller, *Energy Procedia*, 2017, **114**, 220–229.
17 D. Alvarez and J. C. Abanades, *Ind. Eng. Chem. Res.*, 2005, **44**, 5608–5615.
18 A. Iulianelli, S. Liguori, J. Wilcox and A. Basile, *Catal. Rev.: Sci. Eng.*, 2016, **58**, 1–35.
19 M. S. Yancheshmeh, H. R. Radfarnia and M. C. Iliuta, *Chem. Eng. J.*, 2016, **283**, 420–444.
20 B. Dou, C. Wang, Y. Song, H. Chen, B. Jiang, M. Yang and Y. Xu, *Renewable Sustainable Energy Rev.*, 2016, **53**, 536–546.
21 G. Vanga, D. M. Gattia, S. Stendardo and S. Scaccia, *Ceram. Int.*, 2019, **45**, 7594–7605.
22 H. Z. Feng, P. Q. Lan and S. F. Wu, *Int. J. Hydrogen Energy*, 2012, **37**, 14161–14166.
23 G. Wu, C. Zhang, S. Li, Z. Huang, S. Yan, S. Wang, X. Ma and J. Gong, *Energy Environ. Sci.*, 2012, **5**, 8942–8949.
24 M. Broda, A. M. Kierzkowska, D. Baudouin, Q. Imtiaz, C. Coperet and C. R. Müller, *ACS Catal.*, 2012, **2**, 1635–1646.
25 C. Zhao, Z. Zhou, Z. Cheng and X. Fang, *Appl. Catal., B*, 2016, **196**, 16–26.
26 C. Dang, H. Yu, H. Wang, F. Peng and Y. Yang, *Chem. Eng. J.*, 2016, **286**, 329–338.
27 A. Di Giuliano, J. Girr, R. Massacesi, K. Gallucci and C. Courson, *Int. J. Hydrogen Energy*, 2017, **42**, 13661–13680.
28 A. L. García-Lario, G. S. Grasa and R. Murillo, *Chem. Eng. J.*, 2015, **264**, 697–705.
29 M. R. Cesário, B. S. Barros, C. Courson, D. M. A. Melo and A. Kiennemann, *Fuel Process. Technol.*, 2015, **131**, 247–253.
30 H. R. Radfarnia and M. C. Iliuta, *Chem. Eng. Sci.*, 2014, **109**, 212–219.
31 P. Xu, Z. Zhou, C. Zhao and Z. Cheng, *Catal. Today*, 2016, **259**, 347–353.
32 K. D. Dewoolkar and P. D. Vaidya, *Energy Fuels*, 2015, **29**, 3870–3878.
33 C. Dang, Y. Li, S. M. Yusuf, Y. Cao, H. Wang, H. Yu, F. Peng and F. Li, *Energy Environ. Sci.*, 2018, **11**, 660–668.
34 *US Pat.*, US3330697A, 1967.
35 S. Brunauer, P. H. Emmett and E. Teller, *J. Am. Chem. Soc.*, 1938, **60**, 309–319.
36 E. P. Barrett, L. G. Joyner and P. P. Halenda, *J. Am. Chem. Soc.*, 1951, **73**, 373–380.
37 R. A. Dalla Betta, *J. Catal.*, 1974, **34**, 57–60.
38 J. G. Goodwin Jr, *J. Catal.*, 1981, **68**, 227–232.
39 H. Kubicka, *React. Kinet. Catal. Lett.*, 1976, **5**, 223–228.
40 B. Ravel and M. Newville, *J. Synchrotron Radiat.*, 2005, **12**, 537–541.
41 P. Scherrer, *Nachr. Ges. Wiss. Goettingen, Math.-Phys. Kl.*, 1918, 98–100.
42 Q. Zhou, B. J. Kennedy, Z. Zhang, L.-Y. Jang and J. B. Aitken, *Chem. Mater.*, 2009, **21**, 4203–4209.
43 P. G. J. Koopman, A. P. G. Kieboom and H. van Bekkum, *React. Kinet. Catal. Lett.*, 1978, **8**, 389–393.
44 P. Betancourt, A. Rives, R. Hubaut, C. E. Scott and J. Goldwasser, *Appl. Catal., A*, 1998, **170**, 307–314.

45 M. R. Goldwasser, M. E. Rivas, E. Pietri, M. J. Pérez-Zurita, M. L. Cubeiro, L. Gingembre, L. Leclercq and G. Leclercq, *Appl. Catal., A*, 2003, **255**, 45–57.
46 J. C. Abanades and D. Alvarez, *Energy Fuels*, 2003, **17**, 308–315.
47 R. Barker, *J. Appl. Chem. Biotechnol.*, 1973, **23**, 733–742.
48 J. S. Dennis and R. Pacciani, *Chem. Eng. Sci.*, 2009, **64**, 2147–2157.
49 R. Pacciani, C. R. Müller, J. F. Davidson, J. S. Dennis and A. N. Hayhurst, *Can. J. Chem. Eng.*, 2008, **86**, 356–366.
50 J. R. Rostrupnielsen and J. H. B. Hansen, *J. Catal.*, 1993, **144**, 38–49.
51 S. R. Challa, A. T. Delariva, T. W. Hansen, S. Helveg, J. Sehested, P. L. Hansen, F. Garzon and A. K. Datye, *J. Am. Chem. Soc.*, 2011, **133**, 20672–20675.
52 J.-H. Kim, D. J. Suh, T.-J. Park and K.-L. Kim, *Appl. Catal., A*, 2000, **197**, 191–200.